processes

MDPI

Article

Photodiode Signal Patterns: Unsupervised Learning for Laser Weld Defect Analysis

Erkan Caner Ozkat [1,2]

[1] Department of Mechanical Engineering, Faculty of Engineering & Architecture, Recep Tayyip Erdogan University, 53100 Rize, Turkey; erkancaner.ozkat@erdogan.edu.tr
[2] Interdisciplinary Centre for Security Reliability and Trust, Campus Kirchberg, University of Luxembourg, 1855 Kirchberg, Luxembourg

Abstract: Laser welding, widely used in industries such as automotive and aerospace, requires precise monitoring to ensure defect-free welds, especially when joining dissimilar metallic thin foils. This study investigates the application of machine learning techniques for defect detection in laser welding using photodiode signal patterns. Supervised models, including Support Vector Machine (SVM), k-Nearest Neighbors (kNN), and Random Forest (RF), were employed to classify weld defects into sound welds (SW), lack of connection (LoC), and over-penetration (OP). SVM achieved the highest accuracy (95.2%) during training, while RF demonstrated superior generalization with 83% accuracy on validation data. The study also proposed an unsupervised learning method using a wavelet scattering one-dimensional convolutional autoencoder (1D-CAE) network for anomaly detection. The proposed network demonstrated its effectiveness in achieving accuracies of 93.3% and 87.5% on training and validation datasets, respectively. Furthermore, distinct signal patterns associated with SW, OP, and LoC were identified, highlighting the ability of photodiode signals to capture welding dynamics. These findings demonstrate the effectiveness of combining supervised and unsupervised methods for laser weld defect detection, paving the way for robust, real-time quality monitoring systems in manufacturing. The results indicated that unsupervised learning could offer significant advantages in identifying anomalies and reducing manufacturing costs.

Keywords: machine learning; deep learning; laser welding; weld defect; photodiode

Academic Editors: Honggang Chen, Yuan Li and Junyu Guo

Received: 24 November 2024
Revised: 27 December 2024
Accepted: 3 January 2025
Published: 5 January 2025

Citation: Ozkat, E.C. Photodiode Signal Patterns: Unsupervised Learning for Laser Weld Defect Analysis. *Processes* **2025**, *13*, 121. https://doi.org/10.3390/pr13010121

1. Introduction

Laser welding is a cutting-edge joining process that has gained widespread acceptance in industries such as automotive, aerospace, and electronics. This process offers several key advantages, including non-contact operation, single-sided access, and the capability to achieve deep penetration welds with minimal thermal distortion in a fraction of a second [1–3]. Furthermore, its ability to ensure consistent and repeatable welds through automation makes laser welding particularly appealing in industries where high production throughput and reliability are crucial.

Despite its many advantages, quality-related problems can still be encountered in laser welding. The quality of weldments is generally evaluated by measuring a variety of features, which are categorized as (i) surface features (surface spatter, blowout, melt pool width, upper and bottom concavity, and seam discontinuity) and (ii) sub-surface features (lack of connection, over penetration, weld penetration depth, weld connection, porosity, and crack) [4–6]. To ensure a high-quality weld, each feature must comply with the allowance limits defined by industrial standards. Any deviation from these limits

is regarded as a weld defect. These defects not only degrade quality but also increase manufacturing costs due to rework, scrap, and potential safety risks. Therefore, effective monitoring and analysis of the welding process are crucial to ensuring high-quality welds.

As the rapid development of process signals acquisition technologies, both supervised and unsupervised machine learning methodologies related to in-process monitoring and the quality assurance of weld have garnered increasing interest over the past five years [7–9]. There are three primary data sources examined during laser welding: the plasma plume, the molten pool and the keyhole. Depending on the focus of the study, the sensors utilized can be grouped into three main types: optical emissions, acoustic emissions, and charge potential. Photodiodes are the most common sensors adopted for welding anomaly detection for their fast response, low data dimensions, and low costs. They can capture signals from three sources: (i) reflected laser light, (ii) thermal radiation from the weld zone, and (iii) radiation intensity of the plasma [10–12]. Their ability to detect changes in both the intensity and wavelength of light emitted during welding provides instant feedback on the welding conditions.

The integration of supervised learning methods into sensor-driven in-process monitoring frameworks enhances the potential for real-time analysis and defect detection in laser welding processes when sufficient labeled data is available. One notable study by Chianese et al. [13] evaluated the effectiveness of photodiode signals combined with supervised machine learning algorithms for defect classification in remote laser welding of thin foils. They assessed several algorithms, including k-Nearest Neighbors (kNN), Decision Trees (DT), and Support Vector Machines (SVM), achieving promising results in defect detection. The results indicate that these machine learning models can achieve high accuracy rates in defect classification, demonstrating their potential for real-time monitoring applications in industrial settings. Furthermore, the exploration of hybrid methodologies that combine photodiode data with other sensing technologies can significantly enhance defect detection capabilities in laser welding. For instance, Zhang et al. [14] highlight the effectiveness of using real-time spectrometer signals combined with SVM to detect laser welding defects. This integration offers a robust framework for improving weld quality monitoring, paving the way for more reliable and efficient laser welding processes in various industrial applications. Similarly, Deng et al. [15] developed a multi-sensor data fusion system for laser welding process monitoring, where they employed Random Forests (RF) to classify in-process defects based on fused sensor data. Their findings indicated that Random Forests outperformed individual DT in terms of accuracy, showcasing their capability to handle complex interactions among features. However, supervised methods can be limited by the need for large, labeled datasets, which may not always be feasible in industrial settings where defects are rare or labeling is costly and time-consuming [16–19].

To address these challenges, unsupervised learning approaches, which detect deviations in the welding process without requiring labeled data, have gained traction. Unsupervised methods, such as clustering and anomaly detection using autoencoders, deep learning networks have shown promise in identifying anomalies by learning the normal pattern of the process and flagging deviations as potential anomalies [20–24]. The literature also reveals a growing trend towards the application of unsupervised learning methods in analyzing photodiode signal patterns. For instance, Xiao et al. [25] propose a gradient-based unsupervised learning method specifically designed for classifying surface defects in laser welding. This model operates effectively with datasets characterized by a limited number of labels, relying on gradient distributions to identify defects, which is particularly advantageous given the lack of comprehensive datasets in this field. Moreover, Zhang et al. [26] discuss a novel approach for real-time monitoring of penetration states in laser welding processes, specifically for tailor-rolled blanks, using convolutional neural

networks (CNN). The study highlights the effectiveness of deep learning techniques in enhancing the accuracy and efficiency of monitoring systems, addressing the challenges associated with traditional methods. The results demonstrate that the CNN-based monitoring system achieves high accuracy in identifying penetration states, with reported accuracy rates exceeding 95%. Meanwhile, Knaak et al. [27] presents a novel spatio-temporal deep learning architecture designed for real-time defect detection in laser welding processes, specifically optimized for deployment on low power embedded computing boards. The architecture employs CNNs to extract spatial features from individual frames and recurrent neural networks (RNNs) to capture temporal dependencies across frames. This dual approach allows the model to understand both the spatial characteristics of defects and their evolution over time. However, RNNs suffer from vanishing and exploding gradients, limiting their effectiveness in capturing long-term dependencies. Both traditional machine learning and new deep learning networks have been effectively utilized for penetration estimation, achieving a total accuracy rate of 99% in penetration estimation.

Despite advancements in laser welding defect detection, challenges remain especially when joining dissimilar metallic thin foils. Welding dissimilar metals with a laser involves joining materials with differing thermal and mechanical properties, which leads to segregation and precipitates, poor compatibility and miscibility, and poor joint strength. In addition, key product indicators such as penetration depth, keyhole clearance, and part-to-part gap joining that determine the weld quality occur within the welded material and therefore cannot be measured directly during welding. Although supervised machine learning approaches have shown promise in weld defect classification when large, labeled datasets are available, their dependence on extensive labeled data limits their applicability in dynamic, real-world conditions. Unsupervised learning methods, which can analyze unlabeled data to identify anomalies, offer a more flexible and adaptive approach to in-process monitoring [28–30]. However, they may struggle to distinguish between meaningful anomalies and noise, particularly in complex or highly variable industrial environments. Therefore, this study proposes an unsupervised learning network based on photodiode signal patterns to detect anomalies during the laser welding process. The proposed network leverages the strengths of wavelet scattering and a one-dimensional convolutional autoencoder (1D-CAE) to enhance feature extraction and dimensionality reduction. The integration of wavelet scattering enables the capture of both time and frequency domain features, providing a stable and informative representation of non-stationary signals.

The main contributions of this paper are (i) the integration of wavelet scattering and a one-dimensional convolutional autoencoder (1D-CAE), which represents a novel methodological framework for laser welding anomaly detection. Wavelet scattering captures both time and frequency domain features, providing a stable representation of non-stationary photodiode signals, while the 1D-CAE facilitates automatic feature extraction, dimensionality reduction, and reconstruction-based anomaly detection. This combined approach offers a robust solution for monitoring dynamic laser welding processes, particularly in environments with scarce labeled datasets, and (ii) the elimination of reliance on extensive labeled datasets while enabling real-time monitoring, allowing a scalable and efficient solution for defect detection in industrial laser welding applications. By integrating advanced machine learning techniques with real-time data processing, this framework paves the way for smarter manufacturing environments where quality assurance can be achieved proactively and efficiently. Such advancements are crucial for maintaining high standards in production while minimizing downtime and waste, ultimately leading to improved operational efficiency and product quality.

The remainder of the paper is structured as follows: Section 2 presents the experimental setup and outlines the proposed methodologies for weld defect classification using

supervised learning models and anomaly detection through the wavelet scattering 1D-CAE network. Section 3 discusses the findings from both the experiments and the proposed network. Finally, Section 4 provides the conclusions of this study and the directions for future research.

2. Materials & Methods

2.1. Experimental Setup for Laser Welding and Photodiode Signals Acquisition

The quality of a laser-welded joint is typically influenced by key process parameters, such as laser power, welding speed, and laser focus offset. In addition to these parameters, laser incidence angle and part-to-part gap are also relevant process parameters. The incidence angle is important because of the visibility of the welding position and accessibility of the laser scanner head to the workpiece; whereas, the part-to-part gap influences weld defects since if the gap is small porosities and spatters occur, and if it is too large, two parts are unable to weld together.

The primary objective of the present study is to integrate supervised and unsupervised machine learning methodologies into the dataset collected from the laser welding process to identify weld defects. To accomplish this, the experimental data utilized in this study were derived from the study conducted by Chianese et al. [13]. Their research focused on the laser welding of thin copper-steel foils arranged in lap joint configurations, with particular emphasis on two key process parameters: laser power and part-to-part gap. The laser power was adjusted to mimic actual manufacturing conditions where different levels of weld penetration occurred, while changes in spacing between parts were made to reduce possible dimensional errors that could happen during the clamping phase before welding.

In the study, the nLight Compact Fiber Laser (nLight Inc., Camas, WA, USA) with a power output of 3 kW was used for the welding process. The laser power was directed at the samples through a two-dimensional F-theta scanner equipped with telecentric lenses (Scout-200, Laser and Control K-lab., Gunpo-si, Gyeonggi-do, Republic of Korea) operating in continuous mode to ensure precise beam focus on the samples. The welding setups were configured in a lap joint arrangement with a welding length of 40 mm, and the samples measured 70 mm in length and 30 mm in width. Optical emissions from the welding process were monitored using a photodiode-based sensor, Laser Welding Monitoring 4.0 (Precitec GmbH, Gaggenau, Germany), which detected emissions across three distinct wavelength ranges: 300–700 nm for the plasma signal (s_P), 1200–2000 nm for the temperature signal (s_T), and 1020–1090 nm for the back reflection signal (s_R), at a maximum sampling frequency of 50 kHz.

The three geometric features evaluated in every cross-section of the welds were weld penetration depth (DP), throat thickness (TS), and the actual gap between parts. The TS was determined as the minimum distance from the lower corner of the upper material to the weld contour. Based on the measurements, welds were classified into three categories: over-penetration (OP), characterized by a laser mark left on the inspection surface; lack of connection (LoC), where DP is below 0.35 times the thickness of the lower specimen (TL) and TS is below 0.75 times the thickness of the upper specimen (TU); and sound weld (SW), where DP is greater than or equal to 0.35 times TL and TS is greater than or equal to 0.75 times TU. The listed geometrical features are depicted in Figure 1.

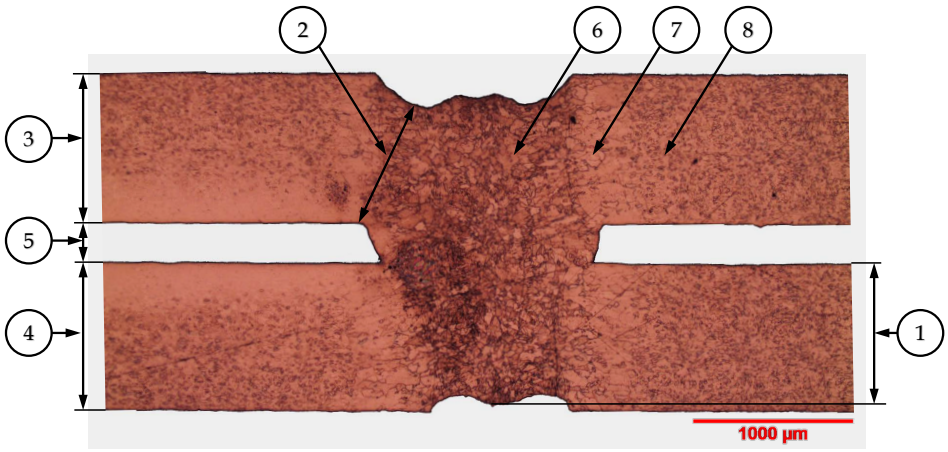

1 Penetration Depth (DP)	2 Throat Thickness (TS)	3 Thickness Upper (TU)	4 Thickness Lower (TL)
5 Part-to-part Gap	6 Fusion Zone	7 Heat Affected Zone	8 Base Metal

Figure 1. The visual representation of the geometrical features.

2.2. Supervised Learning Algorithms for Weld Defect Classification

Photodiode signals were captured with three different channels (s_P, s_T, s_R). Each recording was subsequently preprocessed using signal processing techniques, followed by the development of machine learning models aimed at accurately classifying weld defects. The workflow for developing and evaluating these classification models is illustrated in Figure 2.

Step 1: Data Preprocessing
Data Normalization: Standardize data across channels.
Data Shuffling: Randomize the order of samples.

Step 2: Feature Extraction
Generate Features: Extract features from time and frequency domains for each signal (e.g., crest factor, kurtosis, peak freq).
Feature Selection: Remove non-useful features to improve model performance by focusing on the most relevant features.

Step 3: Data Partitioning
Holdout Cross-Validation: Split the dataset into three parts: 70% for training, 15% for test and 15% for validation.

Step 4: Model Development
Model Training: Train classification machine learning models (i.e., SVM, RF, and kNN) using the training dataset.
Hyperparameter Optimization: Fine-tune model parameters to optimize its performance using the test dataset.

Step 5: Prediction & Evaluation
Make Predictions: Apply the developed models to the validation dataset.
Evaluate Performance: Assess model accuracy using metrics: accuracy, precision, recall, and confusion matrix to determine the best-performing model.

Figure 2. Flowchart of the proposed methodology for classification models.

The first step of the methodology is data preprocessing, in which the raw photodiode signals were initially standardized across all channels to remove scale discrepancies, enabling more uniform input for model training. To further mitigate the risk of overfitting, the dataset was randomized to ensure that the sequence of samples did not influence the training process. The Z-score normalization technique was applied to each channel within every experimental configuration in this study, as presented in Equations (1)–(3).

$$x(t) = \frac{s(t) - \mu}{\sigma} \quad (1)$$

$$\mu = \frac{1}{T}\int_0^T x(t)\,dt \tag{2}$$

$$\sigma = \sqrt{\frac{1}{T}\int_0^T (x(t)-\mu)^2\,dt} \tag{3}$$

where $s(t)$ is the captured signal during weld, $x(t)$ is the normalized signal, μ and σ are the mean value and standard deviation of the normalized signal, respectively.

In Step 2, features were extracted from the normalized signals to serve as informative inputs for the machine learning models. In this study, features were obtained from the time, frequency, and time-frequency domains to best capture the distinguishing characteristics of the normalized signals. Time domain analysis, also known as waveform analysis, involves directly analyzing raw sequences of normalized signals using statistical metrics. These metrics are widely used due to their simplicity of extraction and low computational time. The features used in this study for the time domain analysis include the standard deviation (SD), root-mean-square value (RMS), impulse factor (IF), and clearance factor (CF), which are expressed in Equations (4)–(7), respectively.

$$\mathrm{SD} = \sqrt{\frac{1}{T}\int_0^T (x(t)-\bar{x})^2\,dt} \tag{4}$$

$$\mathrm{RMS} = \sqrt{\frac{1}{T}\int_0^T x(t)^2\,dt} \tag{5}$$

$$\mathrm{IF} = \frac{\max(x(t))}{\mathrm{RMS}} \tag{6}$$

$$\mathrm{CF} = \frac{\max(x(t))}{\left(\frac{1}{T}\int_0^T |x(t)|\,dt\right)^2} \tag{7}$$

The frequency domain analysis, also known as spectrum analysis, is mainly utilized to determine the spectrum of the signal. To analyze the frequency components of the normalized time-domain signals, the fast Fourier transform (FFT) was applied to the normalized time-domain signals to obtain frequency patterns as defined in Equation (8). Unusual peaks in the frequency distribution within the spectrum were thought to be an indication of weld defects. In this study, in the frequency domain analysis, the features of the power spectral density ($P(f)$) such as median frequency (f_{med}), band power (P_{band}), and peak amplitude (P_{peak}) were determined, as defined in Equations (9)–(12), respectively.

$$X(f) = \int_{-\infty}^{\infty} x(t)e^{-j2\pi ft}\,dt \tag{8}$$

$$P(f) = |X(f)|^2 \tag{9}$$

$$f_{\mathrm{med}} = \frac{1}{2}\int_0^{f_{\max}} P(f)\,df \tag{10}$$

$$P_{\mathrm{band}} = \int_{f_1}^{f_2} P(f)\,df \tag{11}$$

$$P_{\mathrm{peak}} = \max(P(f)) \tag{12}$$

The time-frequency domain serves as a critical framework for examining signals that exhibit non-stationary characteristics, where both temporal and frequency information are essential for understanding the dynamics of the signal. A significant instrument for this examination is the spectrogram, which provides a graphical representation of the energy distribution of the signal across time and frequency. To compute the spectrogram of a signal, a window function ($w(\tau - t)$), is applied to isolate sections of the signal around each time point t, and can vary in form (e.g., Gaussian, Hamming, or rectangular) based on the desired time-frequency resolution. The Short-Time Fourier Transform (STFT) then takes the Fourier transform of this windowed segment, yielding the time-frequency representation $S(t, f)$, defined as follows:

$$S(t,f) = \int_{-\infty}^{\infty} x(\tau) w(\tau - t) e^{-j2\pi f \tau} \, d\tau \tag{13}$$

The time-frequency domain features that are focused on in this research are spectral kurtosis (SK), which evaluates the sharpness of the frequency distribution and aids in identifying unusual peaks or outliers that are often linked to defects; spectral skewness (SS), which quantifies the asymmetry of the frequency distribution and suggests possible imbalances within the signal structure; and spectral flatness (SF), which assesses whether the signal is more noise-like or tone-like, assisting in differentiating between normal and defect-related characteristics. These time-frequency features are respectively defined as follows:

$$SK = \frac{\frac{1}{T}\int_0^T (S(t,f) - \mu(f))^4 \, dt}{\left(\frac{1}{T}\int_0^T (S(t,f) - \mu(f))^2 \, dt\right)^2} \tag{14}$$

$$SS = \frac{\frac{1}{T}\int_0^T (S(t,f) - \mu(f))^3 \, dt}{\left(\frac{1}{T}\int_0^T (S(t,f) - \mu(f))^2 \, dt\right)^{3/2}} \tag{15}$$

$$SF = \frac{\exp\left(\frac{1}{T}\int_0^T \log(S(t,f)) \, dt\right)}{\frac{1}{T}\int_0^T S(t,f) \, dt} \tag{16}$$

where $\mu(f)$ is the mean of the spectrogram at frequency f, and T refers to the time interval for each segment. Following the extraction of features from all domains, the minimum redundancy maximum relevance (MRMR) algorithm was utilized to evaluate their significance and eliminate any non-informative or overlapping features. The MRMR algorithm identifies an ideal set of features that are mutually exclusive and maximally distinct, effectively representing the response variable. It achieves this by minimizing redundancy within the feature set while maximizing the relevance of the features to the target variable [31].

Before developing classification models, in Step 3, the extracted features were partitioned into distinct subsets for training, testing, and validation. The training data was used to identify patterns within the data and develop the classification models. The testing data was utilized to adjust the hyperparameters of each classification model. The validation data was used to determine the most effective classification model from the developed ones based on metrics namely accuracy, precision, recall, and the confusion matrix. For this purpose, the extracted features were randomly split into 70% training, 15% testing, and 15% validation data. This systematic approach ensured that the models were robust and generalizable, minimizing the risk of overfitting while maximizing their predictive performance on unseen data.

In Step 4, supervised machine learning models; namely Support Vector Machine (SVM) [32], Random Forest (RF) [33], and k-Nearest Neighbor (kNN) [34], were developed using the training dataset to classify sound welds and weld defects based on photodiode

signals. To improve the classification performance of these models, hyperparameters were carefully fine-tuned using the test dataset. This process involved systematically adjusting the parameters and determining the optimal configuration to achieve the highest classification accuracy possible.

In Step 5, these models were applied to an unseen validation dataset to generate predictions, which were then compared against the actual class labels. The performance of the models was evaluated using accuracy, precision, recall, and the confusion matrix. These metrics provided a comprehensive assessment of the ability of models to correctly classify the photodiode signals, enabling the identification of the best-performing model.

2.3. Unsupervised Learning Network for Weld Defect Detection

This study proposes an unsupervised learning network based on photodiode signal patterns to detect anomalies during the laser welding process. The proposed network combines the advantages of wavelet scattering (WS) and the one-dimensional convolution autoencoder (1D-CAE) to capture both time and frequency domain information in photodiode signals. This architecture, which is depicted in Figure 3, enables automatic feature extraction and dimensionality reduction while reconstructing the input signal patterns to identify deviations indicative of defects. The anomaly detection capability of this architecture is based on reconstruction error. By comparing the original input signals with their reconstructed versions from the decoder, an anomaly score can be calculated. High reconstruction errors indicate potential anomalies in the input data, allowing for the effective detection of outliers or unusual patterns in sequential signals.

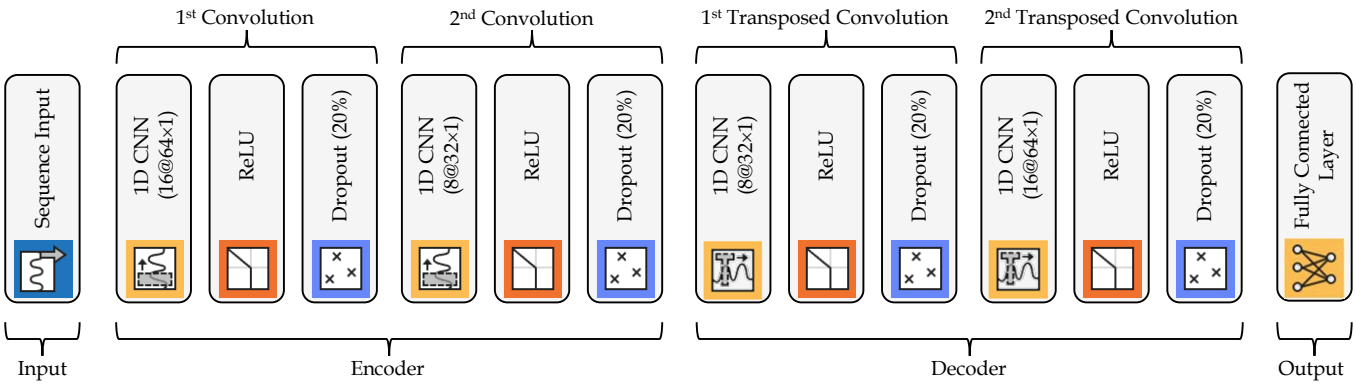

Figure 3. The network structure of the 1D convolution autoencoder.

The input layer of the proposed network utilizes wavelet scattering to preprocess the photodiode signals. Wavelet scattering is selected as the initial layer due to its automatic feature extraction capabilities [35,36], its stability in representing non-stationary signals [37,38], and its ability to capture both multi-scale and multi-frequency features of the input data [39]. The key benefits of the wavelet scattering method in this study are as follows: (i) it provides a time-frequency representation, capturing both temporal and spectral dynamics crucial for identifying patterns associated with varying welding conditions; (ii) it enables multi-scale analysis, allowing for consistent detection of welding defects, such as over-penetration or lack of connection, which manifest as features at varying scales and frequencies in the signal, thereby enhancing the robustness of the defect detection process; and (iii) it facilitates dimensionality reduction by generating stable coefficients that retain essential information, thereby improving the efficiency and performance of subsequent models, such as the 1D-CAE used for anomaly detection. This preprocessing phase significantly improves the performance of the subsequent layers, as the obtained

features are the essential features that enable the network to learn complex patterns and relationships in the input signal.

In mathematical terms, wavelet scattering starts by convolving the input signal $x(t)$, in this case, normalized photodiode signals, with a set of wavelets $\psi_\lambda(t)$, where λ represents the scale and frequency parameters. This yields a series of high-frequency components, $x(t) \otimes \psi_\lambda(t)$, which capture localized variations in the signal. To enhance stability and suppress noise, the modulus of each filtered component is taken, and then each output is further convolved with a second wavelet filter, effectively creating a cascade of wavelet transformations. At each m layer of the cascade, the scattering coefficients $S_m x(t)$ are calculated by applying a pooling operation, usually averaging through a low-pass filter $\phi_m(t)$. Finally, the mathematical formulation of wavelet scattering is as follows:

$$S_m x(t) = |||x(t) \otimes \psi_{\lambda_1}(t)| \otimes \psi_{\lambda_2}(t)| \cdots \otimes \psi_{\lambda_m}| \otimes \phi_m \tag{17}$$

The 1D-CAE is a deep learning network architecture that utilizes the one-dimensional convolutional neural network (1D-CNN) within its convolutional layers. While the 1D-CAE structure is similar to traditional autoencoders, which consist of an encoder and a decoder, it has a notable distinction: weight sharing. In the 1D-CAE, weights are shared across all connections in each layer, allowing the model to maintain the spatial structure of the input by preserving relative feature locations. This is crucial for anomaly detection in sequential data, as the local structure of the signal may contain important information about potential anomalies. The shared weights and one-dimensional convolutional structure thus enable the 1D-CAE to reconstruct the input signal based on a reduced latent representation, capturing spatial dependencies and enhancing the model capacity to identify deviations in the underlying patterns of process data.

The encoder part of the CAE contains two 1D-CNN layers, each of which is followed by a Rectified Linear Unit (ReLU) activation to introduce non-linearity and a 20% dropout layer to prevent overfitting. The first convolutional layer employs 64 filters, each with a length of 16, and applies a stride of 2. The stride refers to how much the filter shifts along the input sequence with each step, resulting in an output that is approximately half the size of the original input. The second convolutional layer uses 32 filters with a size of 8 and with stride of 2. The 1D-CNN in the encoding stage is defined as follows:

$$z_j^c = f\left(\sum_m W_{m,j}^c * x_m^{c-1} + b_j^c\right) \tag{18}$$

where z_j^c denotes the resulting feature corresponding to the j-th channel with the c-th convolutional layer; b_j^c is the bias for the j-th feature; $W_{m,j}^c$ denotes the convolutional weight matrix; M represents the input channel data; $*$ denotes the convolution operation; the term x_m^{c-1} refers to the feature map from the m-th input channel with the c-th convolutional layer, capturing the channel's data input; and f denotes the ReLU activation function.

The decoder mirrors the encoder structure with transposed convolutional layers to upsample and reconstruct the original signal. These transposed convolutional layers are configured with the same parameters as the convolutions (64 filters of size 16 with a stride of 2, 32 filters of size 8 with a stride of 2), with ReLU activations and 20% dropout applied after each layer to maintain robustness and control overfitting. The decoding stage reconstructs the output dimensions by reversing the dimensionality reduction from the encoding stage, which is expressed by the following calculation:

$$\hat{x}_j^c = f\left(\sum_m \hat{W}_{m,j}^c \odot x_m^{c-1} + \hat{b}_j^c\right) \tag{19}$$

where $\hat{x}_j^c$ represents the output feature corresponding to the j-th channel with the c-th deconvolution layer; $\hat{b}_j^c$ indicates the bias associated with the j-th feature; $\hat{W}_{m,j}^c$ denotes the convolutional weight matrix; M represents the input channel data; and $\odot$ denotes the deconvolution operation.

A fully connected layer with three output units follows the decoder layer, acting as the final feature mapping layer and producing predictions or classifications based on the model's application. Lastly, a truncation function ensures the output dimensions match the target by trimming any excess padding, thereby preserving the original sequence length and dimensional integrity. The training process involves updating the weights and biases parameters of the network using the Adam optimization algorithm until the maximum number of 500 epochs is reached. The training data will be shuffled after each epoch to prevent the model from overfitting to the training set. The loss function between the reconstructed signal ($\hat{X}_i$) and input signal (X_i) is defined by the mean squared error as follows:

$$Loss = \frac{1}{n}\sum_{i=1}^{n}(X_i - \hat{X}_i)^2 \tag{20}$$

2.4. Anomaly Detection Mechanism

The methodology for implementing the proposed wavelet scattering 1D-CAE network consists of five key steps. The first step involved preprocessing the acquired photodiode signals using Z-score normalization and defining wavelet scattering parameters to prepare the data for robust feature extraction. In the second step, wavelet scattering is applied to the normalized signal to generate scattering coefficients, which capture invariant and noise-resistant features. These coefficients serve as inputs to the 1D-CAE, which is illustrated in Figure 3. The third step involves training the 1D-CAE network using a set of training data in an iterative loop, using mini-batches and the Adam optimizer to minimize the reconstruction loss, with test data employed to monitor and save the best-performing model. The trained network can accurately reconstruct the input signal data with minimal deviation. When a faulty signal is presented and reconstructed using the trained network, the difference between the reconstructed signal and the original faulty signal becomes significantly larger. This study employed the same training, test, and validation datasets utilized for the weld defect classification. However, for the purpose of anomaly detection, instances of lack of connectivity (LoC) and overpenetration (OP), previously categorized as weld defects, were reclassified as anomalies. Finally, the postprocessing step evaluates the reconstruction loss on validation data, producing the trained model and reconstructed signals as outputs. An anomaly score is computed based on the reconstruction loss, which is the difference between the input and reconstructed signals. A threshold is determined for the reconstruction loss, beyond which a signal is classified as an anomaly, indicative of a potential defect. This threshold is determined using a value-based method on a user-defined fraction of expected anomalies. The reconstruction losses from all training windows are computed and sorted in ascending order, and the threshold is set at the loss corresponding to the $1-\gamma$th percentile γ is the set fraction. Any signal with a reconstruction loss exceeding this threshold is classified as an anomaly. The pseudocode of the wavelet scattering 1D-CAE network is shown in Algorithm 1.

Algorithm 1 The pseudocode of the wavelet scattering 1D convolution autoencoder with threshold calculation.

Require: Load time-series photodiode signals s_P, s_T, s_R
Require: Define constants: Sampling Frequency fs, Window Size w_s
Require: Define Wavelet Scattering architecture
Require: Define 1D-CAE architecture
for *channel* $=$ 1 to 3 **do** ▷ Process signals s_P, s_T, s_R individually
  Normalize the input signal
  Segment signal into w_s-length windows (e.g., 100 ms intervals)
  Apply wavelet scattering transform to each window
  Extract features from wavelet scattering coefficients
  Split features into training, test, and validation datasets
  Initialize 1D-CAE network
Require: Define training hyperparameters: optimizer (Adam), maximum epochs E, batch size B, shuffle strategy (shuffle every epoch)
  for *epoch* $t = 1$ to E **do** ▷ Training Loop
    Shuffle training data randomly
    Divide training data into mini-batches of size B
    for each mini-batch B in training data **do**
      Perform forward pass: Reconstruct features using the 1D-CAE
      Compute reconstruction loss:

$$\text{Loss}_b = ||\text{Features} - \text{Reconstructed Features}||^2$$

      Backpropagate the loss and update network weights using the Adam optimizer
    end for
    Compute reconstruction loss on test data
    Save the network if the test reconstruction loss improves
  end for
  Compute reconstruction losses $\mathcal{L}$ for all training windows
  Sort the reconstruction losses in ascending order: $\mathcal{L}_{\text{sorted}}$
  Calculate the detection threshold τ using contamination fraction γ:

$$\text{Index} = \lceil (1 - \gamma) \times N \rceil$$

$$\tau = \mathcal{L}_{\text{sorted}}[\text{Index}]$$

▷ e.g., $\gamma = 0.01$ ensures 1% of windows are flagged as anomalies
  Evaluate the trained model on validation data
  Flag windows with reconstruction loss $> \tau$ as anomalies
end for

3. Results & Discussions

3.1. Photodiode Signal Patterns

The welding experiments were performed with varying laser power levels from 600 to 1500 W and part-to-part gaps from 0 to 300 µm. The photodiode captured three distinct signals throughout each experiment: s_P, s_T, and s_R. Both the hardware and software gains were adjusted to limit the signals within the range of 0 to 10 V. Figure 4 demonstrates the normalized amplitude variation of each signal to compare and highlight their cyclic behaviour.

These observed signal patterns suggest that sound welds (SW) maintain stable signal intensities and consistent temporal profiles across all emission ranges, indicating balanced laser-material interaction, optimal heat input, and uniform plasma formation. When compared to over-penetration (OP), the correlation of signals reveals that OP exhibits increased intensity in the plasma signal (s_P) and temperature signal (s_T), suggesting excessive heat input and deeper penetration. In contrast, the lack of connection (LoC) displays a different correlation pattern with the signals. The signals recorded from LoC exhibit a similar pattern to those recorded from SW. In addition, the comparison between SW and LoC reveals the decreasing intensities in s_P and s_T, as well as the increasing back reflection in s_R that may indicate weak welding and weld defects. Implementing advanced monitoring technologies, such as real-time data analysis and machine learning algorithms, can further enhance welding processes by allowing for adaptive process parameter adjustment that responds to changing welding conditions on the fly.

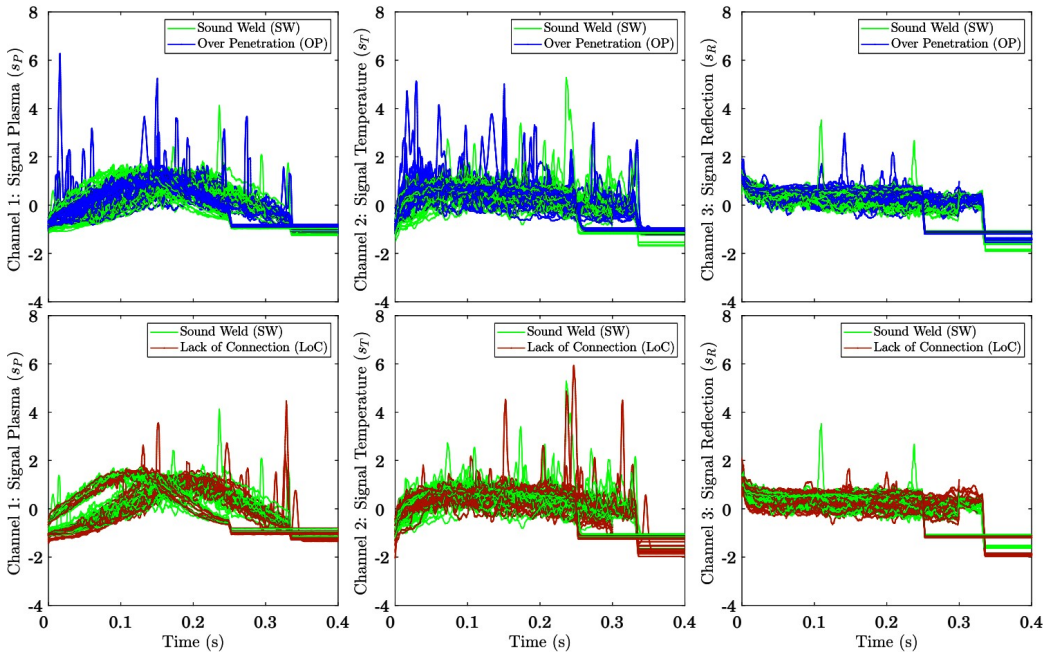

Figure 4. Photodiode signals (normalized) recorded during the welding process are categorized as over-penetration (OP), lack of connection (LoC), and sound weld (SW).

3.2. Comparison of Supervised Learning Methods Performance

The confusion matrices in Figure 5 display the classification performance of the SVM, kNN, and RF models for both the training and the validation datasets across the three welding quality classes: Lack of Connection (LoC), Over-Penetration (OP), and Sound Weld (SW). For the training dataset, all models exhibited robust performance in classifying SW, suggesting effective learning of optimal weld characteristics. However, classification accuracy for LoC and OP defects varied across models. The SVM model demonstrated superior classification accuracy, particularly for LoC, with only 2 misclassifications. While the kNN model provided consistent overall classification, it exhibited the lowest accuracy among the models. Nevertheless, all three supervised learning methods achieved high accuracy rates on the training dataset, with SW consistently identified by all models. In summary, SVM and RF models excelled in identifying sound welds, whereas kNN offered balanced performance across classes but with slightly higher error rates.

During the validation phase, a noticeable decrease in performance was noted for all models. The SVM model accurately classified 5 instances of LoC, making 2 misclassifications and displaying satisfactory performance for the OP class, achieving 5 correct predictions with 1 error. In the case of the SW class, 9 instances were correctly identified, with 2 misclassifications. The kNN model exhibited a major decline, accurately identifying 5 LoC instances while misclassifying 2. For the OP class, it made 4 correct predictions alongside 2 errors. The SW class achieved 9 correct identifications but faced 2 misclassifications. Likewise, the RF model produced stable results, classifying 5 instances of LoC correctly with 2 misclassifications. The OP class demonstrated enhanced results, with 5 instances classified correctly. The SW class retained strong performance with 10 correct predictions and just 1 error. Overall, the RF model demonstrates superior performance in terms of balanced classification across the three categories, while the SVM and kNN models perform comparably with a slightly higher rate of misclassification between LoC and OP.

Table 1 presents the calculated classification metrics, including accuracy, precision, sensitivity, and specificity, for each model on both the training and validation datasets. Accuracy measures the overall correctness of predictions as the ratio of correct predictions to total instances, while precision indicates the proportion of true positive predictions

among all positive predictions. Sensitivity measures the ability of the model to correctly identify positive cases, which is crucial for early detection in applications. On the other hand, specificity assesses the accuracy of the model in recognizing negative cases, which is important for avoiding the misclassification of negatives.

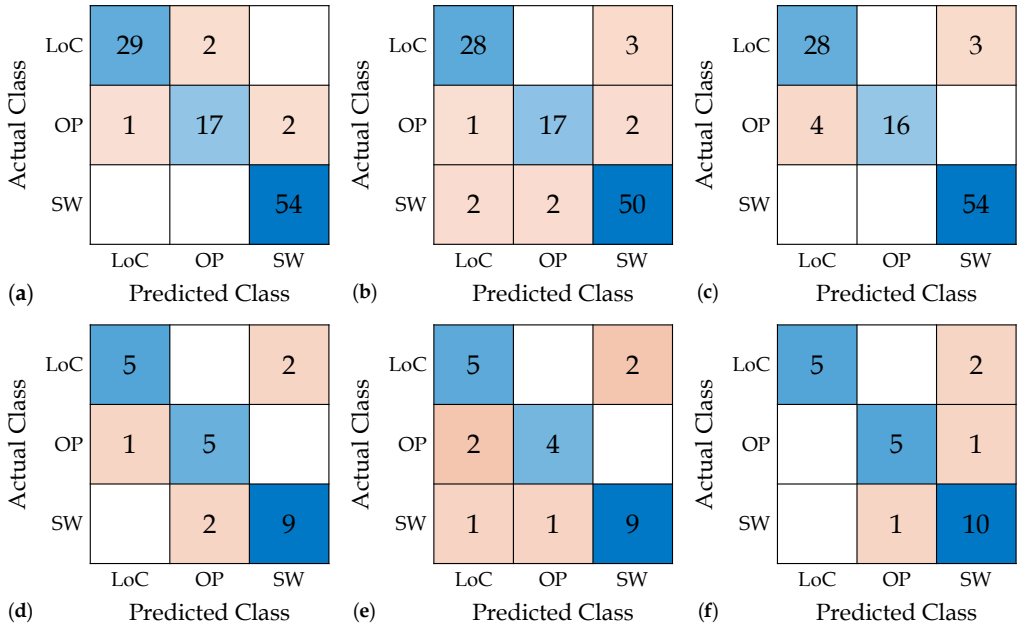

Figure 5. Confusion matrices for (**a**) SVM, (**b**) kNN and (**c**) RF models associated with the training dataset; and, (**d**) SVM, (**e**) kNN and (**f**) RF models associated with the validation dataset, respectively.

For the training dataset, the SVM model achieved the highest accuracy (0.952) among the three models, with precision values of 0.966 for LoC, 0.894 for OP, and 0.964 for SW. Sensitivity scores were similarly high, especially for SW at 1. The specificity was also consistently above 0.95 for all classes, indicating strong discriminative performance. The kNN model had an accuracy of 0.904, slightly lower than SVM. Precision for LoC and OP stood at 0.903 and 0.894, respectively, while SW had a precision of 0.909. Sensitivity scores for LoC and OP were 0.903 and 0.85, respectively, with SW at 0.925. Specificity remained robust, particularly for OP at 0.976. The RF model achieved an accuracy rate of 0.933. Precision values included 0.875 for LoC, a perfect 1 for OP, and 0.947 for SW. The sensitivity for LoC was 0.903, and it reached 1 for SW. Specificity was high for all classes, with perfect specificity for OP.

On the other hand, for the validation dataset, the SVM model shows perfect precision (1.000) and specificity (1.000) for the OP class, reflecting its reliability in minimizing false positives for this category. However, its sensitivity for LoC (0.714) is slightly lower than RF, suggesting some limitations in detecting all true positives for this class. Moreover, the kNN model displays comparatively lower performance, with the lowest sensitivity for the OP class (0.666). While its precision for the SW class is identical to RF and SVM (0.818), its specificity for the OP class (0.944) is slightly inferior to RF. This indicates that kNN may struggle to generalize effectively across certain anomalies. Among the models, the RF classifier achieves the highest overall accuracy of 0.833, followed by SVM (0.792) and kNN (0.750). RF demonstrates superior performance across most class-specific metrics, particularly excelling in sensitivity for the SW class (0.909) and specificity for the LoC class (0.941). This indicates RF's robustness in correctly identifying anomalies and distinguishing between normal and anomalous behavior. Overall, the comparative analysis of the models reveals that the RF model exhibited stable and balanced performance, making it the most

suitable model for this application. The kNN model faced the most significant decrease in performance, suggesting that it may be more sensitive to variations in the dataset.

Table 1. The performance comparison of three machine learning models for welding classification.

Dataset	Model	Accuracy	Precision			Sensitivity			Specificity		
			LoC	OP	SW	LoC	OP	SW	LoC	OP	SW
Training	SVM	0.952	0.966	0.894	0.964	0.935	0.850	1.000	0.986	0.976	0.960
	kNN	0.904	0.903	0.894	0.909	0.903	0.850	0.925	0.959	0.976	0.901
	RF	0.933	0.875	1.000	0.947	0.903	0.800	1.000	0.945	1.000	0.941
Validation	SVM	0.792	0.625	1.000	0.818	0.714	0.833	0.818	0.824	1.000	0.846
	kNN	0.750	0.625	0.800	0.818	0.714	0.666	0.818	0.823	0.944	0.846
	RF	0.833	0.833	0.833	0.833	0.714	0.833	0.909	0.941	0.944	0.846

An analysis of variance (ANOVA) was conducted to determine if the differences in mean performance among the classifiers were statistically significant. The analysis was based on the results from ten-fold cross-validation. The ANOVA revealed a p-value below 0.05, confirming that the performance differences between the classifiers were significant. To further investigate, pairwise t-tests were performed to identify the best classifier with statistical significance. The results showed a significant difference between SVM and kNN ($p = 0.022$), indicating that SVM performed better. However, no significant differences were found between SVM and RF ($p = 0.093$) or between kNN and RF ($p = 0.156$). These findings suggest that while SVM outperformed kNN, its performance was similar to RF, and kNN and RF performed comparably.

3.3. Anomaly Detection Based on the Proposed Unsupervised Learning Method

The proposed unsupervised learning method for anomaly detection, which integrates wavelet scattering and a one-dimensional convolutional autoencoder (1D-CAE), was applied to the photodiode signal data collected during the laser welding process. The wavelet scattering was generated with a 100 ms invariance scale and a 50 kHz sampling rate for 0.4 s. Two layers of filters were set and four filters were employed in the first layer, while a single filter was utilized in the second layer, resulting in a feature matrix comprising 29 distinct scattering coefficients and 51 samples per scattering coefficient per photodiode channel. The extracted wavelet scattering coefficients were subsequently fed into 1D-CAE for anomaly detection.

The previously employed training, testing, and validation datasets were also utilized for anomaly detection. Nevertheless, in this study, instances of lack of connection (LoC) and overpenetration (OP), categorized as weld defects, were jointly classified as anomalies for anomaly detection. The anomaly detection capability of the proposed 1D-CAE network was evaluated using reconstruction loss as the primary indicator. It was computed by comparing the original input signal to the output of the network. Figure 6 displays the cumulative distribution function (CDF) and a histogram of the reconstruction loss for all signals. The threshold that separates normal and abnormal signals is determined by the proportion of data points in the dataset that are considered abnormal by the network. The choice of threshold is influenced by the acceptable risk level for the application; lower thresholds are favored in safety-critical systems to detect subtle anomalies, while higher thresholds may be used in less critical contexts to minimize noise. The threshold value was set to 0.025 because it effectively separates normal and anomalous data based on the reconstruction loss distribution observed during training, allowing the 95th percentile of normal instances to be correctly identified. Moreover, as indicated in Figure 6, the threshold determined by the 1D-CAE network exceeds the loss values for the majority of normal data samples but remains below a significant number of abnormal data losses, indicating the potential presence of anomalies.

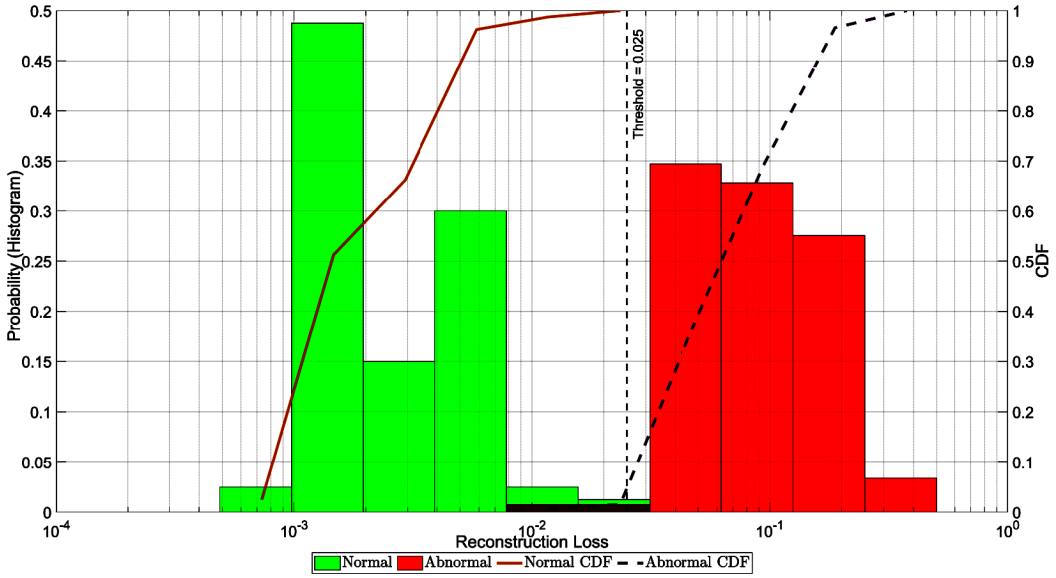

Figure 6. The distribution of reconstruction losses for normal and abnormal data.

Figures 7 and 8 illustrate examples of the original input photodiode signals and the detected anomalies for each channel. These anomalies are highlighted by the red lines, contrasting with the green lines representing the input signal. Channels s_P, s_T and s_R exhibit anomalies with varying intensities and timing, reflecting the impact of physical parameters measured by each channel. The general trend in anomalies is that there are sudden changes in signal amplitude or significant deviations from the signal normal baseline in the early stages of the welding process. By determining the conditions under which anomalies occur, it was seen that early anomalies occur in the LoC cases and sudden changes occur in the OP cases.

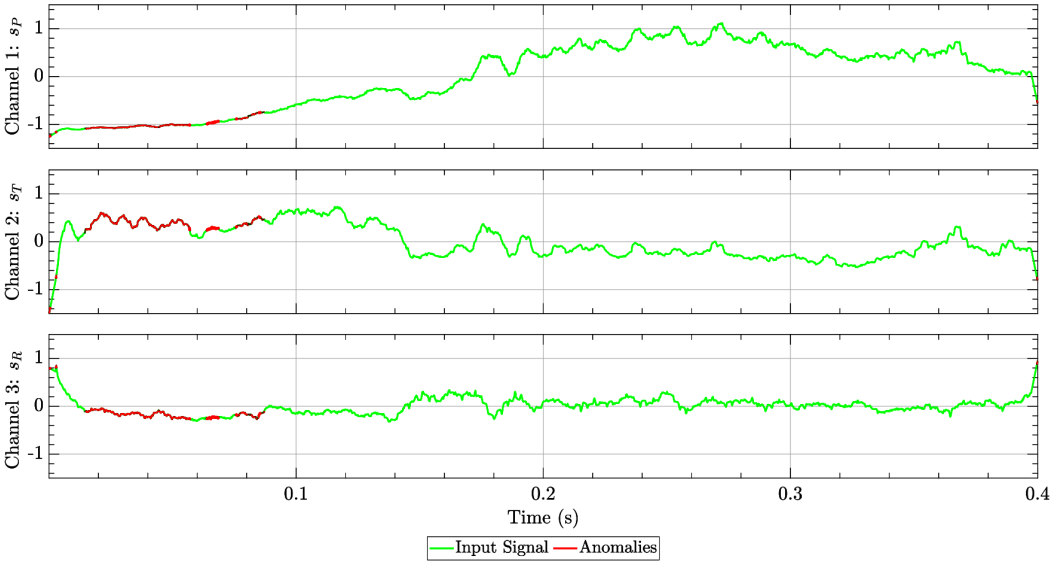

Figure 7. Detected anomalies in photodiode signals for the given input signal: Lack of Connection (LoC) case.

Photodiode signals are directly related to the optical emissions generated during the welding process. In the case of LoC, the optical emission level is quite low since sufficient contact cannot be established between the materials being welded. This situation can be considered to explain the anomalies observed, especially at the beginning of the welding process. On the other hand, in the case of OP, a more intense optical emission is produced

due to excessive heat. This situation leads to significant fluctuations and abnormal peaks in the photodiode signals. In addition, the anomalies in different photodiode channels can be seen at different times and with different intensities due to the differences in the physical parameters measured by each channel.

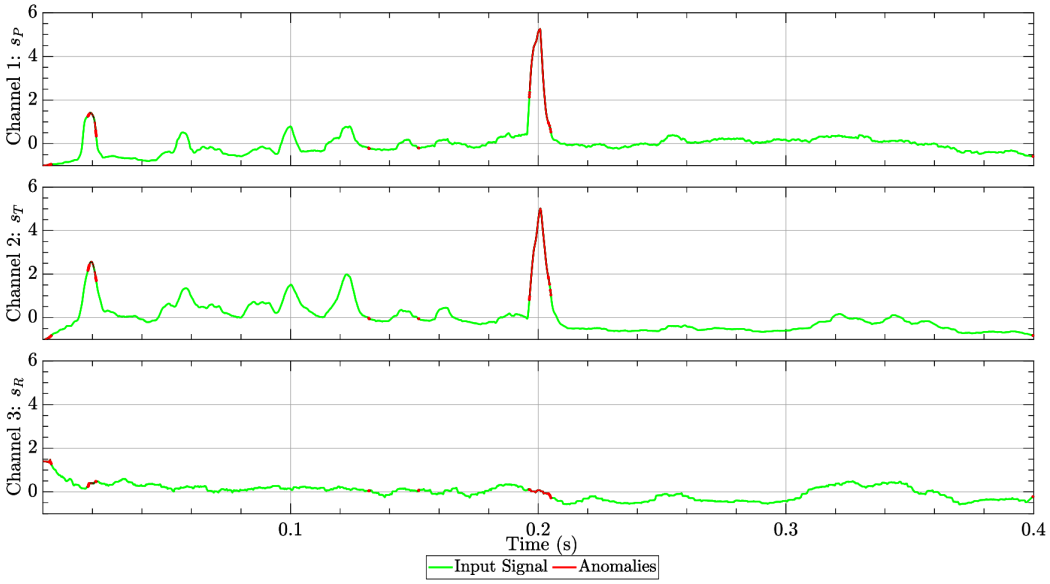

Figure 8. Detected anomalies in photodiode signals for the given input signal: Overpenetration (OP) case.

The confusion matrices shown in Figure 9 demonstrate how well the proposed wavelet scattering 1D-CAE performs in detecting anomalies in the training and validation datasets. In the training dataset (Figure 5a), the model successfully detected 51 abnormal samples and 47 normal samples, with only a few errors: 3 false negatives and 4 false positives, indicating strong learning ability and reliability. In the validation dataset (Figure 5b), the model obtained similarly good results, accurately classifying 11 abnormal samples and 10 normal samples, with just 2 false negatives and 1 false positive.

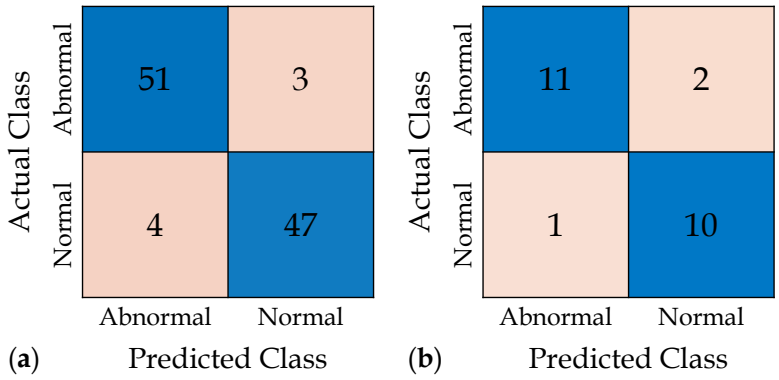

Figure 9. Confusion matrix for (**a**) the training dataset and (**b**) the validation dataset, respectively.

The effectiveness of the proposed anomaly detection method was assessed using metrics; namely, accuracy, precision, sensitivity, and specificity as summarized in Table 2. During the training phase, the model achieved an accuracy of 93.3%, with a balanced precision of 92.7% for detecting abnormalities and 94.0% for normal patterns. Sensitivity values further indicate the ability of the network to detect anomalies (94.4%) and normal data (92.1%) effectively. Specificity metrics also confirm the low false-positive rate for both classes, at 92.1% and 94.4%, respectively. Similarly, in the validation phase, the model

maintained a competitive accuracy of 87.5%, showing slightly reduced but acceptable precision for abnormal (91.6%) and normal (83.3%) classes. These findings underscore the robustness of the proposed network in identifying weld anomalies without the need for labeled training data. In summary, the proposed unsupervised learning approach demonstrated reliable performance in detecting anomalies associated with weld defects, providing a valuable tool for in-process monitoring and quality assurance in laser welding.

Table 2. The performance of the wavelet scattering 1D-CAE network for anomaly detection.

Dataset	Accuracy	Precision		Sensitivity		Specificity	
		Abmornal	Normal	Abnormal	Normal	Abnormal	Normal
Training	0.933	0.927	0.940	0.944	0.921	0.921	0.944
Validation	0.875	0.916	0.833	0.846	0.909	0.909	0.846

The proposed methods, when applied to real-time industrial settings, necessitate careful consideration of computational requirements and scalability. To support real-time processing, the infrastructure must be robust, utilizing high-performance hardware such as GPUs or specialized edge devices that can handle the intensive computational demands of the algorithms. These systems should be optimized for low-latency performance, ensuring fast decision-making through parallel computing or algorithmic simplifications. Furthermore, addressing scalability is crucial, as industrial applications generate vast amounts of data that need to be processed and analyzed in real time. Techniques such as distributed computing, cloud-based systems, or efficient data compression can help manage the large data streams typical of industrial environments. The proposed methods must also integrate seamlessly with existing industrial systems, requiring compatibility with common communication protocols and supporting connectivity with various sensor networks. Depending on the specific application, a hybrid approach that combines edge and cloud computing may offer the best balance of low latency and computational power, with edge devices handling immediate processing and the cloud supporting more complex computations. Additionally, energy efficiency must be prioritized to ensure long-term operational sustainability, particularly in IoT-heavy environments. Finally, the methods must be designed to be fault-tolerant and reliable, incorporating redundancy, error detection, and recovery mechanisms to maintain system uptime and ensure robustness in dynamic industrial operations.

4. Conclusions

This study successfully applied both supervised and unsupervised machine learning techniques to analyze photodiode signals for laser weld defect classification and anomaly detection, offering a robust framework for quality assurance in laser welding processes. The key findings of the research are as follows:

1. Distinct Signal Patterns for Weld Defects:
    - Sound welds (SW) maintained stable signal intensities and consistent temporal profiles across all emission ranges, indicative of balanced laser-material interaction and uniform plasma formation.
    - Over-penetration (OP) was associated with higher plasma (s_P) and temperature (s_T) signal intensities, reflecting excessive heat input and deeper penetration.
    - Lack of connection (LoC) exhibited lower plasma and temperature signal intensities and increased back reflection (s_R), indicating weak weld integrity.
2. Supervised Learning Performance:

- Among the supervised methods, Support Vector Machine (SVM) achieved the highest accuracy (95.%) on the training dataset, excelling in classifying sound welds (SW), lack of connection (LoC), and over-penetration (OP).
- On the validation dataset, Random Forest (RF) emerged as the most generalizable model, achieving an accuracy of 83.3%, with balanced precision, sensitivity, and specificity across all defect classes.
- The k-Nearest Neighbors (kNN) model, while slightly less accurate, demonstrate

3. Unsupervised Anomaly Detection:
    - The wavelet scattering one-dimensional convolutional autoencoder (1D-CAE) demonstrated strong performance in detecting anomalies, achieving accuracies of 93.3% (training) and 87.5% (validation).
    - Wavelet scattering effectively captured robust features from photodiode signals in both time and frequency domains, enabling the model to distinguish normal signals from anomalies without requiring labeled data.
    - The method demonstrated low false-positive and false-negative rates, making it suitable for real-world industrial applications where labeled datasets are scarce or unavailable.

These results highlight the potential of merging supervised and unsupervised learning methods to improve the monitoring of laser weld quality. Supervised approaches such as SVM and RF provide excellent accuracy for identifying defects when labeled data is present, whereas the unsupervised 1D-CAE offers a scalable and effective means of spotting anomalies in unlabeled data. The future work will aim to incorporate the proposed methods into real-time monitoring systems, addressing key challenges such as latency issues and hardware requirements. To ensure low latency, the framework utilizes computationally efficient components, including wavelet scattering for feature extraction and a lightweight 1D-CAE architecture for anomaly detection. Optimization techniques like model quantization and pruning will be employed to further reduce computational overhead without sacrificing performance. Additionally, the use of parallel processing on industrial-grade hardware, such as GPUs and edge-computing devices, enables the system to process high-frequency photodiode signals (up to 50 kHz) in real time with minimal latency. Regarding hardware requirements, platforms with adequate processing power offer compact, energy-efficient solutions that meet the computational demands of real-time monitoring. These platforms also provide sufficient memory bandwidth to handle multiple photodiode signal channels simultaneously, ensuring effective monitoring in high-throughput welding environments. For applications. it is planned to explore deploying pre-trained models on embedded systems or microcontrollers. This approach involves offline model training, followed by deployment for in-line monitoring, ensuring adaptability and efficiency in diverse manufacturing settings. Such advancements will not only refine defect detection capabilities but also contribute to the widespread adoption of intelligent automation in manufacturing, making it more efficient, reliable, and cost-effective.

Funding: This research received no external funding.

Data Availability Statement: The data utilized in this study has been obtained from the work conducted by Chianese et al. [13], and it is freely available through this link: https://zenodo.org/records/5115087, accessed on 23 November 2024.

Conflicts of Interest: The author declares no conflicts of interest.

Abbreviations

The following abbreviations are used in this manuscript:

CAE	Convolutional AutoEncoder
1D-CNN	One-dimensional Convolutional Neural Network
WS	Wavelet Scattering
SVM	Support Vector Machine
kNN	k Nearest Neighbor
RF	Random Forest
LoC	Lack of Connection
OP	Over Penetration
SW	Sound Weld
DP	Penetration Depth
TS	Throat Thickness
TU	Thickness Upper
TL	Thickness Lower
s_P	Signal Plasma
s_T	Signal Temperature
s_R	Signal Reflection

References

1. Ozkat, E.C.; Franciosa, P.; Ceglarek, D. Laser dimpling process parameters selection and optimization using surrogate-driven process capability space. *Opt. Laser Technol.* **2017**, *93*, 149–164. [CrossRef]
2. Kawahito, Y.; Mizutani, M.; Katayama, S. Investigation of high-power fiber laser welding phenomena of stainless steel. *Trans. JWRI* **2007**, *36*, 11–15.
3. Buongiorno, D.; Prunella, M.; Grossi, S.; Hussain, S.M.; Rennola, A.; Longo, N.; Di Stefano, G.; Bevilacqua, V.; Brunetti, A. Inline defective laser weld identification by processing thermal image sequences with machine and deep learning techniques. *Appl. Sci.* **2022**, *12*, 6455. [CrossRef]
4. Ozkat, E.C.; Franciosa, P.; Ceglarek, D. Development of decoupled multi-physics simulation for laser lap welding considering part-to-part gap. *J. Laser Appl.* **2017**, *29*, 012003. [CrossRef]
5. Sun, T.; Ademi, S.; Mishra, S.; Varsani, D.; McMahon, R.; Ceglarek, D.; Franciosa, P. Joining thin copper wire and copper busbar by remote laser welding for electric motor assembly: Impact of welding parameters and pre-welding surface treatment. *Sci. Technol. Weld. Join.* **2024**, *29*, 337–346. [CrossRef]
6. Mohan, A.; Ceglarek, D.; Franciosa, P.; Auinger, M. Numerical study of beam oscillation and its effect on the solidification parameters and grain morphology in remote laser welding of high-strength aluminium alloys. *Sci. Technol. Weld. Join.* **2023**, *28*, 362–371. [CrossRef]
7. Cai, W.; Wang, J.; Jiang, P.; Cao, L.; Mi, G.; Zhou, Q. Application of sensing techniques and artificial intelligence-based methods to laser welding real-time monitoring: A critical review of recent literature. *J. Manuf. Syst.* **2020**, *57*, 1–18. [CrossRef]
8. Wu, S.; Kong, W.; Feng, Y.; Chen, P.; Cheng, F. Penetration prediction of narrow-gap laser welding based on coaxial high dynamic range observation and machine learning. *J. Manuf. Process.* **2024**, *110*, 91–100. [CrossRef]
9. Shevchik, S.A.; Le-Quang, T.; Farahani, F.V.; Faivre, N.; Meylan, B.; Zanoli, S.; Wasmer, K. Laser welding quality monitoring via graph support vector machine with data adaptive kernel. *IEEE Access* **2019**, *7*, 93108–93122. [CrossRef]
10. You, D.; Gao, X.; Katayama, S. Review of laser welding monitoring. *Sci. Technol. Weld. Join.* **2014**, *19*, 181–201. [CrossRef]
11. Lu, R.; Lou, M.; Xia, Y.; Huang, S.; Li, Z.; Lyu, T.; Wu, Y.; Li, Y. Machine learning-based in-process monitoring for laser deep penetration welding: A survey. *Eng. Appl. Artif. Intell.* **2024**, *137*, 109059. [CrossRef]
12. Huang, Z.; Yan, J.; Zhang, J.; Han, C.; Peng, J.; Cheng, J.; Wang, Z.; Luo, M.; Yin, P. Deep Learning-Based Fatigue Strength Prediction for Ferrous Alloy. *Processes* **2024**, *12*, 2214. [CrossRef]
13. Chianese, G.; Franciosa, P.; Nolte, J.; Ceglarek, D.; Patalano, S. Characterization of photodiodes for detection of variations in part-to-part gap and weld penetration depth during remote laser welding of copper-to-steel battery tab connectors. *J. Manuf. Sci. Eng.* **2022**, *144*, 071004. [CrossRef]
14. Zhang, Y.; Gao, X.; You, D.; Zhang, N. Data-driven detection of laser welding defects based on real-time spectrometer signals. *IEEE Sensors J.* **2019**, *19*, 9364–9373. [CrossRef]
15. Deng, F.; Huang, Y.; Lu, S.; Chen, Y.; Chen, J.; Feng, H.; Zhang, J.; Yang, Y.; Hu, J.; Lam, T.L.; et al. A multi-sensor data fusion system for laser welding process monitoring. *IEEE Access* **2020**, *8*, 147349–147357. [CrossRef]

16. Yalcin-Ozkat, G.; Ersan, R.H.; Ulger, M.; Ulger, S.T.; Burmaoglu, S.; Yildiz, I.; Algul, O. Design, synthesis, and computational studies of benzimidazole derivatives as new antitubercular agents. *J. Biomol. Struct. Dyn.* **2023**, *41*, 2667–2686. [CrossRef] [PubMed]
17. Ceryan, N.; Ozkat, E.C.; Korkmaz Can, N.; Ceryan, S. Machine learning models to estimate the elastic modulus of weathered magmatic rocks. *Environ. Earth Sci.* **2021**, *80*, 448. [CrossRef]
18. Ozturk, U.K.; Abdioglu, M.; Ozkat, E.C.; Mollahasanoglu, H. Extended 2-D magnetic field modeling of linear motor to investigate the magnetic force parameters of high-speed superconducting maglev. *IEEE Trans. Appl. Supercond.* **2023**, *33*, 1–8. [CrossRef]
19. Cruz, Y.J.; Rivas, M.; Quiza, R.; Beruvides, G.; Haber, R.E. Computer vision system for welding inspection of liquefied petroleum gas pressure vessels based on combined digital image processing and deep learning techniques. *Sensors* **2020**, *20*, 4505. [CrossRef] [PubMed]
20. Ozkat, E.C. Vibration data-driven anomaly detection in UAVs: A deep learning approach. *Eng. Sci. Technol. Int. J.* **2024**, *54*, 101702. [CrossRef]
21. Ozkat, E.C.; Bektas, O.; Nielsen, M.J.; la Cour-Harbo, A. A data-driven predictive maintenance model to estimate RUL in a multi-rotor UAS. *Int. J. Micro Air Veh.* **2023**, *15*, 17568293221150171. [CrossRef]
22. Ozkat, E.C.; Abdioglu, M.; Ozturk, U.K. Machine learning driven optimization and parameter selection of multi-surface HTS Maglev. *Phys. C Supercond. Its Appl.* **2024**, *616*, 1354430. [CrossRef]
23. Chen, S.; Yu, J.; Wang, S. One-dimensional convolutional auto-encoder-based feature learning for fault diagnosis of multivariate processes. *J. Process Control* **2020**, *87*, 54–67. [CrossRef]
24. You, W.; Shen, C.; Guo, X.; Jiang, X.; Shi, J.; Zhu, Z. A hybrid technique based on convolutional neural network and support vector regression for intelligent diagnosis of rotating machinery. *Adv. Mech. Eng.* **2017**, *9*, 1687814017704146. [CrossRef]
25. Xiao, S.; Liu, Z.; Yan, Z.; Wang, M. Grad-MobileNet: A Gradient-Based Unsupervised Learning Method for Laser Welding Surface Defect Classification. *Sensors* **2023**, *23*, 4563. [CrossRef] [PubMed]
26. Zhang, Z.; Li, B.; Zhang, W.; Lu, R.; Wada, S.; Zhang, Y. Real-time penetration state monitoring using convolutional neural network for laser welding of tailor rolled blanks. *J. Manuf. Syst.* **2020**, *54*, 348–360. [CrossRef]
27. Knaak, C.; von Eßen, J.; Kröger, M.; Schulze, F.; Abels, P.; Gillner, A. A spatio-temporal ensemble deep learning architecture for real-time defect detection during laser welding on low power embedded computing boards. *Sensors* **2021**, *21*, 4205. [CrossRef] [PubMed]
28. Ji, C.; Hou, Z.; Dai, W. A Lightweight Safety Helmet Detection Algorithm Based on Receptive Field Enhancement. *Processes* **2024**, *12*, 1136. [CrossRef]
29. Ding, H.; Gao, Y.; Hu, F.; Guo, Y.; Liu, C. Deep Integration and Innovation Development in the Logistics and Manufacturing Industries and Their Performances: A Case Study of Anhui Province, China. *Processes* **2024**, *12*, 1867. [CrossRef]
30. Du, H.; Li, Q.; Guan, Z.; Zhang, H.; Liu, Y. An Improved Lightweight YOLOv8 Network for Early Small Flame Target Detection. *Processes* **2024**, *12*, 1978. [CrossRef]
31. Peng, H.; Long, F.; Ding, C. Feature selection based on mutual information criteria of max-dependency, max-relevance, and min-redundancy. *IEEE Trans. Pattern Anal. Mach. Intell.* **2005**, *27*, 1226–1238. [CrossRef] [PubMed]
32. Goyal, D.; Choudhary, A.; Pabla, B.; Dhami, S. Support vector machines based non-contact fault diagnosis system for bearings. *J. Intell. Manuf.* **2020**, *31*, 1275–1289. [CrossRef]
33. Liu, K.; Hu, X.; Zhou, H.; Tong, L.; Widanage, W.D.; Marco, J. Feature analyses and modeling of lithium-ion battery manufacturing based on random forest classification. *IEEE/ASME Trans. Mechatronics* **2021**, *26*, 2944–2955. [CrossRef]
34. Zhang, S.; Li, X.; Zong, M.; Zhu, X.; Wang, R. Efficient kNN classification with different numbers of nearest neighbors. *IEEE Trans. Neural Netw. Learn. Syst.* **2017**, *29*, 1774–1785. [CrossRef] [PubMed]
35. Liu, F.; Xia, S.; Wei, S.; Chen, L.; Ren, Y.; Ren, X.; Xu, Z.; Ai, S.; Liu, C. Wearable electrocardiogram quality assessment using wavelet scattering and LSTM. *Front. Physiol.* **2022**, *13*, 905447. [CrossRef] [PubMed]
36. Bondyra, A.; Kołodziejczak, M.; Kulikowski, R.; Giernacki, W. An acoustic fault detection and isolation system for multirotor UAV. *Energies* **2022**, *15*, 3955. [CrossRef]
37. Bruna, J.; Mallat, S. Invariant scattering convolution networks. *IEEE Trans. Pattern Anal. Mach. Intell.* **2013**, *35*, 1872–1886. [CrossRef]
38. Toma, R.N.; Gao, Y.; Piltan, F.; Im, K.; Shon, D.; Yoon, T.H.; Yoo, D.S.; Kim, J.M. Classification framework of the bearing faults of an induction motor using wavelet scattering transform-based features. *Sensors* **2022**, *22*, 8958. [CrossRef] [PubMed]
39. Sharma, M.; Lodhi, H.; Yadav, R.; Acharya, U.R. Sleep disorder identification using wavelet scattering on ECG signals. *Int. J. Imaging Syst. Technol.* **2024**, *34*, e22980. [CrossRef]